

Atomistic understanding of capacity loss in $LiNiO_2$ for high-nickel Li-ion batteries: First-principles study

Shuai Peng(彭率), Li-Juan Chen(陈丽娟), Chang-Chun He(何长春), and Xiao-Bao Yang(杨小宝)

Citation: Chin. Phys. B, 2024, 33 (**5**): 058201. DOI: 10.1088/1674-1056/ad2a72
Journal homepage: http://cpb.iphy.ac.cn; http://iopscience.iop.org/cpb

What follows is a list of articles you may be interested in

Degradation mechanism of high-voltage single-crystal $LiNi_{0.5}Co_{0.2}Mn_{0.3}O_2$ cathode material

Na Liu(柳娜)
Chin. Phys. B, 2023, 32 (**12**): 128202. DOI: 10.1088/1674-1056/ad01a3

Synthesis and electrochemical performance of La_2CuO_4 as a promising coating material for high voltage Li-rich layered oxide cathodes

Fuliang Guo(郭福亮), Jiaze Lu(卢嘉泽), Meihua Su(苏美华), Yue Chen(陈约), Jieyun Zheng(郑杰允), Liang Yin(尹良), and Hong Li(李泓)
Chin. Phys. B, 2023, 32 (**8**): 088201. DOI: 10.1088/1674-1056/acd2bc

A novel calculation strategy for optimized prediction of the reduction of electrochemical window at anode

Guochen Sun(孙国宸), Jian Gao(高健), and Hong Li(李泓)
Chin. Phys. B, 2023, 32 (**7**): 078201. DOI: 10.1088/1674-1056/accd51

Structural, electronic, and Li-ion mobility properties of garnet-type $Li_7La_3Zr_2O_{12}$ surface: An insight from first-principles calculations

Jing-Xuan Wang(王靖轩), Bao-Zhen Sun(孙宝珍), Mei Li(李梅), Mu-Sheng Wu(吴木生), and Bo Xu(徐波)
Chin. Phys. B, 2023, 32 (**6**): 068201. DOI: 10.1088/1674-1056/acc05d

Neutron-based characterization techniques for lithium-ion battery research

Enyue Zhao(赵恩岳), Zhi-Gang Zhang(张志刚), Xiyang Li(李西阳), Lunhua He(何伦华), Xiqian Yu(禹习谦), Hong Li(李泓), Fangwei Wang(王芳卫)
Chin. Phys. B, 2020, 29 (**1**): 018201. DOI: 10.1088/1674-1056/ab5d07

Atomistic understanding of capacity loss in $LiNiO_2$ for high-nickel Li-ion batteries: First-principles study

Shuai Peng(彭率)[1,2], Li-Juan Chen(陈丽娟)[1], Chang-Chun He(何长春)[1], and Xiao-Bao Yang(杨小宝)[1,2,†]

[1] *School of Physics and Optoelectronics, South China University of Technology, Guangzhou* 510000, *China*
[2] *Center of Excellence for Advanced Materials, Dongguan* 523808, *China*

(Received 19 December 2023; revised manuscript received 9 February 2024; accepted manuscript online 19 February 2024)

Combining the first-principles calculations and structural enumeration with recognition, the delithiation process of $LiNiO_2$ is investigated, where various supercell shapes are considered in order to obtain the formation energy of Li_xNiO_2. Meanwhile, the voltage profile is simulated and the ordered phases of lithium vacancies corresponding to concentrations of 1/4, 2/5, 3/7, 1/2, 2/3, 3/4, 5/6, and 6/7 are predicted. To understand the capacity decay in the experiment during the charge/discharge cycles, deoxygenation and Li/Ni antisite defects are calculated, revealing that the chains of oxygen vacancies will be energetically preferrable. It can be inferred that in the absence of oxygen atom in high delithiate state, the diffusion of Ni atoms is facilitated and the formation of Li/Ni antisite is induced.

Keywords: Li-ion battery, ground state, formation energy, oxygen vacancy, Li/Ni antisite

PACS: 82.47.Aa, 63.20.dk, 31.15.es **DOI:** 10.1088/1674-1056/ad2a72

1. Introduction

The extensive usage of fossil fuels has resulted in global warming and its severe ramifications, and it is urgent to change the way of consuming energy to avoid the negative effects on the environment. To achieve zero emissions, renewable energy sources are crucial and the intermittent production necessitates specific requirements for energy storage materials. Therefore, batteries in the future will have a broader application in several products,[1,2] where the criteria for battery performance will also become more rigorous. Layered materials are widely used in the lithium batteries, since $LiCoO_2$ and $LiNiO_2$ are characterized as cathode materials due to their high energy densities and high voltage plateaus. With the same structure, $LiCoO_2$ is the first to be successfully commercialized due to its good stability, while $LiNiO_2$ performs particularly poorly in terms of stability. However, the natural resource reserves of Co are limited, and there is an urgent need to find high energy density electrode materials that do not contain Co.[3]

There is still a significant controversy about the performance of $LiNiO_2$ material, although experimental studies on the delithiation phase diagram have been carried out for nearly three decades. The diversity of the results origins from the delithiation process, corresponding to different phase diagrams of the ground state as a function of Li concentration.[4] The capacity of this material decreases rapidly with the increase of the number of charge–discharge cycles, which may be due to several reasons: lattice instability, cation disorder, phase transition, microcrack expansion, and oxygen precipitation from the electrodes.[5–12] Note that oxygen precipitation and cation disorder are considered to be the main causes.[13] To improve the performance, a large proportion of manganese[14] and aluminum[15] have been used to replace Ni in the materials, which will consequently reduce the energy density due to the low Ni content. In order to develop high-Ni electrode materials with high stabilities and energy densities, an in-depth study of $LiNiO_2$ materials is required.

Theoretically, there is a lack of the mechanism of cation disorder and oxygen precipitation. In this paper, the phase diagram and structural stability of the Li_xNiO_2 system are systematically investigated by using first-principles calculations. All the configurations of Li_xNiO_2 in the supercells of small size are calculated by enumeration, and some configurations with high symmetry are selected in the larger supercells. The ordered structures are determined, which are used to simulate their voltage profiles. In addition, the effect of the concentration of oxygen vacancies is investigated and the oxygen vacancies are found to exist in Li_xNiO_2 in chains' arrangement, which makes the antisites energetically preferrable. Our study contributes to a more in-depth understanding of the stability of $LiNiO_2$ materials.

2. Computational method

Spin-polarized calculations in the framework of density functional theory (DFT) are performed by using the Vienna *ab initio* simulation package (VASP)[16–18] with projector augmented wave pseudopotentials.[19,20] The exchange–correlation functionals are approximated by the generalized gradient approximation (GGA) in the the PBE form.[21] Since the ordinary GGA generalization cannot accurately describe the 3d orbital forces of Ni, the GGA+U approach[22] is adopted to deal with the strong correlation effects of the d-orbital electrons, with the value of U set to 6 for Ni, ac-

†Corresponding author. E-mail: scxbyang@scut.edu.cn

© 2024 Chinese Physical Society and IOP Publishing Ltd

cording to previous literature.[23] The energy cutoff of plane wave is 500 eV and structures are fully relaxed until the force is less than 0.02 eV/Å. The Brillouin zone is sampled with allowed spacing between k-points in 0.3 Å^{-1}, with Γ-centered Monkhorst–Pack k-point grid for high-throughput calculations.

To generate the possible stable candidates, the structures of alloy generation and recognition (SAGAR) code is used, which was developed in our group.[24] For the supercells with 2–7 times the volume of primitive cell, all the unique configurations are enumerated. For the larger cells, our attention is paid only to the candidates with high symmetry (corresponding to a small number of Wyckoff positions) to reduce the computational cost. The method provides a strategy of screening candidates with high symmetry from binary alloys based on the number of Wyckoff positions, where candidates with a small number of Wyckoff positions exhibit higher symmetry and become stable structures with higher probability as confirmed in our previous study.[25] Also, we have done the test in Li_xNiO_2 systems. As shown in Fig. S3 in the supporting information, the formation energy of candidates with high symmetry tends to be either higher or lower than that with low symmetry structure.

Regarding the x values in deoxygenation and antisite defects, we focus on lithium concentrations of 0.25, 0.5, 0.75, and 1, considering the experimental results of the stability phase coupled with its high symmetry. Due to this heightened symmetry, the number of deoxygenation structures generated from this phase is relatively small, allowing us to explore its deoxygenation properties at a lower computational cost.

In order to in depth study the stability of $LiNiO_2$, we use lobster code to conduct the crystal orbital hamilton population (COHP) analyses.[26] The pairs of atoms whose distance is between 1.8 Å and 2.2 Å are calculated.

3. Results and discussion

To study the stabilities of Li_xNiO_2, first, we adopt the atomistic model of bulk $LiNiO_2$ and determine the ordered structure of Li_xNiO_2. In Subsection 3.2, we focus on the formation energy of Li_xNiO_2 and predict the voltage profile. We discuss the effect of oxygen defect and Li concentration on the structural stability of Li/Ni antisite defect in Subsection 3.3.

3.1. Li_xNiO_2 system modeling and candidate structures

To simulate the delithiation process of $LiNiO_2$, a space group with rhombohedral symmetry ($R\bar{3}m$) is adopted as shown in Fig. 1(a). The interlayer atoms are arranged according to Li–O–Ni–O, where Li is at the 3a site, Ni is at the 3b site, and O is at the 6c site. The lattice parameters of the optimized primitive cell are $a = b = c = 5.065$ Å; $\alpha = \beta = \gamma = 33.2°$. Expanding the primitive cells and generating candidate structures with SAGAR, a total of 629 delithiated candidate structures are obtained eventually, and the number of candidate structures corresponding to different supercells is shown in the Supporting information.

The ground state structures of Li_xNiO_2 are determined according to the compositional phase diagram, where the ordered phases appear at $x = 1/4$, 2/5, 3/7, 1/2, 2/3, 3/4, 5/6, and 6/7. This is partly consistent with previously predicted ordering of 0.25, 0.33, 0.4, 0.5, 0.6, 0.75, and 0.83.[27] or 0.125, 0.25, 0.33, 0.5, 0.6, 0.625, 0.67, 0.75, 0.83, and 0.875.[28]

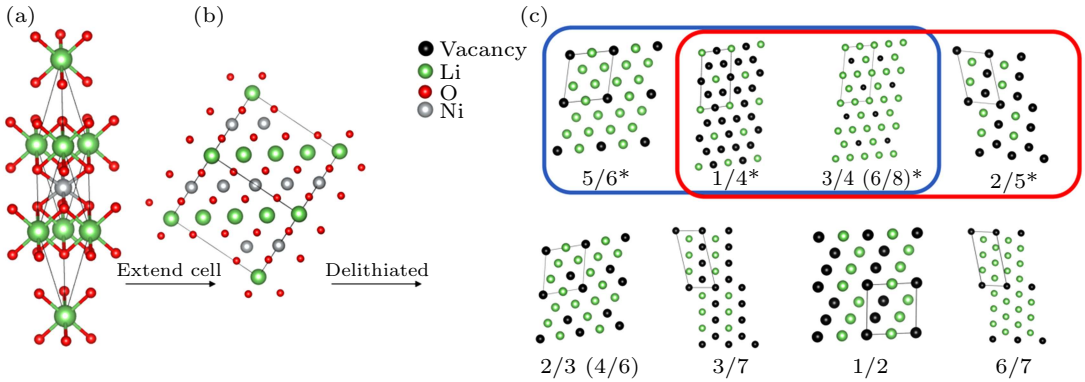


Fig. 1. (a) Structure of primitive cell. (b) Structure of supercell. (c) Li–vacancy ordering in Li sublattice. Li ions and vacancies are denoted as green solid dots and black solid dots, respectively. The structures in blue rectangle were reported by Ceder[28] and those in the red rectangle were reported by Sicolo.[4]

3.2. Formation energy and voltage profile

According to the total energy from the first-principles calculations, we obtain the formation energy to characterize the thermodynamic stabilities of the delithiated structure Li_xNiO_2 at different Li–vacancy distributions:

$$\Delta E[\text{formation}] = E[Li_xNiO_2] - xE[LiNiO_2] - (1-x)E[NiO_2], \quad (1)$$

where $E[Li_xNiO_2]$ is the energy of the delithiated candidate structure, $E[LiNiO_2]$ is the energy of the $LiNiO_2$, $E[NiO_2]$ is the energy of the NiO_2, x is the concentration of Li, and all of the above energy values are averaged to a unit molecule.

As shown in Fig. 2(a), the formation energy values of Li_xNiO_2 are less than 0, which implies that these candidate structures are thermodynamically stabilized. It also indicates

that the Li–Li interaction is repulsive, which leads to an ordered distribution of Li–vacancies (as shown in Fig. 1(c)). In the formation energy diagram of Li_xNiO_2, the convex hull profile and vertexes are obtained, and the convex hull connects all the vertexes, which correspond to the ordered Li–vacancy distribution. When the Li concentration of a structure is in the middle of two vertexes, there will be a phase separation corresponding to a mixed superposition of the two ordered phases next to it. Our calculations show that the ground state will appear at $x = 1/4$, 2/5, 3/7, 1/2, 2/3, 3/4, 5/6, 6/7.

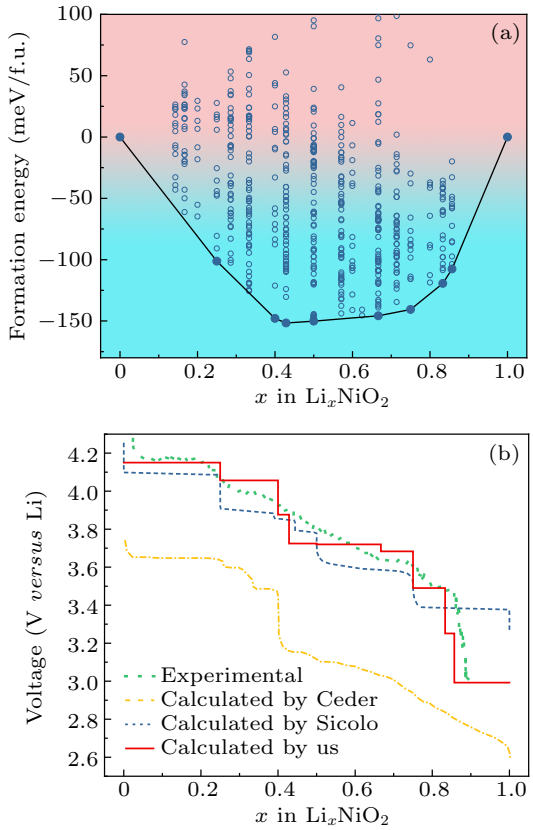


Fig. 2. (a) Calculated formation energy of Li_xNiO_2 convex hulls. (b) Comparison between experimental and calculated voltage profiles, with green solid line representing Sicolo's experimental voltage profile,[4] red solid line denoting our calculated voltage profile, blue line referring to Sicolo's calculated voltage profile[4] at 300 K, and yellow line being Ceder's calculated voltage profile.[27]

The equilibrium voltage of an electrochemical lithium battery depends on the difference in Li chemical potential between the anode material and cathode material.[29] According to the ground state structures found, we can calculate the average chemical potential, *i.e.*, the voltage of Li_xNiO_2 at 0 K between different concentrations as given below:

$$\begin{aligned}\bar{V} = &(E[\mathrm{Li}_{x_1}\mathrm{NiO_2}] - E[\mathrm{Li}_{x_2}\mathrm{NiO_2}] \\ &+ (x_2 - x_1)E[\mathrm{Li}])/(x_2 - x_1),\end{aligned} \tag{2}$$

where $\bar{V}$ is the average voltage between Li concentrations of x_1 and x_2, specifically, $\bar{V}$ is the average voltage between the energy of the ground state structure for Li concentration of x_1 and the energy of the ground state structure for Li concentration of x_2, and E[Li] is the energy of the Li bulk structure. All the above energy values are averaged to a unit molecule.

Figure 2(b) shows the comparison between computationally simulated voltage profile and the experimentally measured one, demonstrating that the simulated voltage profile is accurately consistent with the observed ground state structure.

3.3. Oxygen and Li/Ni antisite defect stability

In order to exclude the interactions between oxygen vacancies attributed to periodic boundary conditions, we choose a supercell with 64 atoms with the furthest first nearest neighbor.[30] Using SAGAR, we generate and calculate all its candidate structures at 1, 2 oxygen vacancies. To discuss the effect of concentration of Li and oxygen vacancy distribution, we focus on the candidate structures of $Li_{16}Ni_{16}O_{30}$, $Li_{12}Ni_{16}O_{30}$, $Li_8Ni_{16}O_{30}$, and $Li_4Ni_{16}O_{30}$. We can describe their stabilities by using the oxygen vacancy formation energy as follows:

$$\begin{aligned}&\Delta E_{n\mathrm{O_{vac}}}[\mathrm{Li}_{16-x}\mathrm{Ni}_{16}\mathrm{O}_{32-n}] \\ &= (E[\mathrm{Li}_{16-x}\mathrm{Ni}_{16}\mathrm{O}_{32-n}] \\ &\quad - E[\mathrm{Li}_{16-x}\mathrm{Ni}_{16}\mathrm{O}_{32}] + 0.5nE[\mathrm{O_2}])/n,\end{aligned} \tag{3}$$

where n is the number of oxygen vacancies and E is the total energy, n = 1–4, and $x = 0$, 4, 8, 12.

The results show that these structures have the same tendencies in forming double oxygen vacancies, specifically, the formation energy is lowest when the oxygen vacancies are spaced at both sides of the Ni (*i.e.* at distance of 3.9 Å in Fig. 3(a)) and form chains (see Fig. S2 in the supporting information). Notably, $Li_{0.75}NiO_2$ has a $C2/m$ space group and that distance of oxygen vacancy is 3.75 Å. Also, as shown in Fig. 3(a), oxygen vacancy formation energy decreases with lithium concentration decreasing, implying that the exfoliation of Li promotes the formation of O vacancies. In addition, we calculate the candidate structures at 3,4 oxygen vacancies to further discuss the effect of concentration of Li and oxygen vacancy. To consider the computational cost, we restrict the distance between oxygen vacancies and select the structures with lower Wyckoff sites. The results show that oxygen vacancies still tend to form chains, with two oxygen vacancy chains formed when there are four oxygen vacancies in the cell. Therefore, we conclude that the oxygen vacancies in $LiNiO_2$ are distributed in chains.

Figure 3(b) shows the formation energy values varying with concentration of oxygen vacancies for different Li/O concentrations. When concentration of Li decreases from 1 to 0.25, the formation energy of oxygen vacancies will decrease for those with the same oxygen concentration, indicating that the concentration of Li could affect the stability of oxygen va-

cancy. It also shows that the formation of the first oxygen vacancy in the system is difficult. However, once an oxygen vacancy has appeared in the system, the formation energy of the subsequent oxygen vacancies decreases by 0.2 eV–0.4 eV. The value will be near 0.4 eV for $Li_{0.25}NiO_2$ and thus the formation of oxygen vacancies is susceptible, providing a reasonable explanation of the oxygen loss in Li_xNiO_2 during charging and discharging cycles.

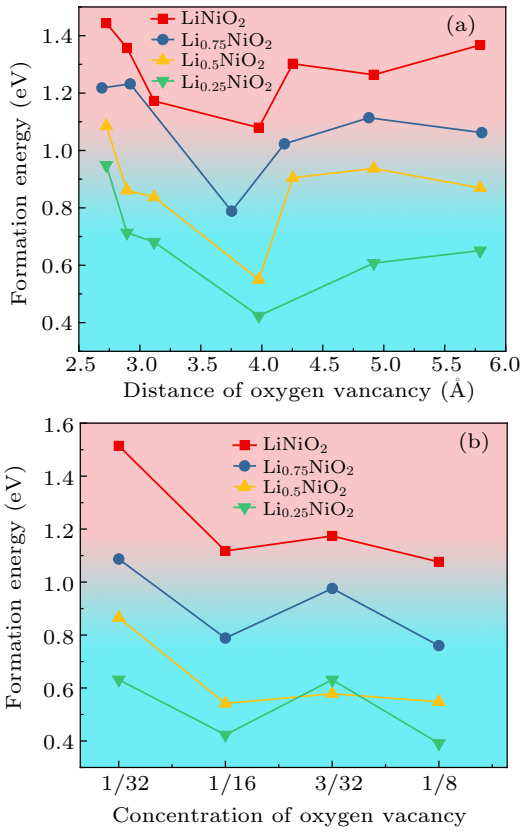


Fig. 3. (a) Plots of oxygen vacancy formation energy *versus* the distance of oxygen vacancy for double oxygen vacancy candidate structures, with the data kept only for the structures with the lowest energy at different distances of the oxygen vacancy, red squares being for $LiNiO_2$, blue circle for $Li_{0.75}NiO_2$, green lower triangle for $Li_{0.5}NiO_2$, and purple rhombus for $Li_{0.25}NiO_2$; (b) plots of oxygen vacancy formation energy versus Li and O concentration, with red square being for $LiNiO_2$, blue circle for $Li_{0.75}NiO_2$, yellow upper triangle for $Li_{0.5}NiO_2$, and green lower triangle for $Li_{0.25}NiO_2$.

In the following, we investigate the effect of the creation of chain oxygen vacancies on the formation energy of Li/Ni antisite. We exchange the positions of Ni atoms next to oxygen vacancies with their nearest-neighbor, next-nearest-neighbor Li atoms and calculate their energy values (see Fig. 4(b)), and assess the possibility of the antisite by the difference between the energy before forming the antisite and that after forming the antisite:

$$\Delta E\,[\mathrm{Li/Ni}] = E\,[\mathrm{defect}] - E[\mathrm{perfect}], \tag{4}$$

where E[defect] is the energy of $LiNiO_{2-x}$ which formed a Li/Ni antisite and E[perfect] is the energy of $LiNiO_{2-x}$.

Figure 4(a) displays that the plots of formation energy versus concentration of oxygen vacancies for different Li/Ni antisites, indicating that the formation energy decreases with the oxygen vacancy concentration increasing. When the concentration of oxygen vacancies reaches 12.5%, the formation energy values of $Li_{0.25}NiO_2$ and $Li_{0.5}NiO_2$ are both close to zero, and the antisite defects will be easy to appear. Although the Li/Ni antisite formation energy values of $LiNiO_2$ and $Li_{0.75}NiO_2$ are small too, the antisite defects are not easily generated in the system for the high formation energy of oxygen vacancies. So, the following conclusion can be made: the system is easy to the form the antisite defects at low lithium concentrations.

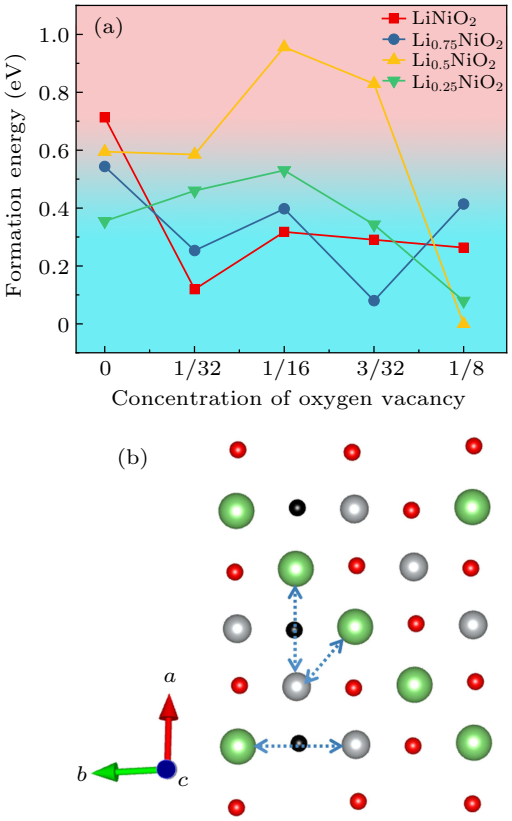


Fig. 4. (a) Variations of Li/Ni antisite formation energy with oxygen vacancy concentration, with red square being for $LiNiO_2$, blue circle for $Li_{0.75}NiO_2$, grey upper triangle for $Li_{0.5}NiO_2$, green lower triangle for $Li_{0.25}NiO_2$. (b) Several ways of constructing Li/Ni antisites, with black spheres for oxygen vacancy, green spheres for Li atoms, silver spheres for Ni atoms, red spheres for O atoms, double arrows referring to that the positions of the atoms on both sides are exchanged to calculate the Li/Ni antisite.

In order to better explain this phenomenon, we conduct the crystal orbital Hamilton population (COHP) analyses to investigate the bonding characteristics. As shown in Fig. S4 in the supporting information, the energy interval from −2.8 eV to 4 eV is dominated by the antibonding contributions in Ni–O bonds, while the Li–O bonds contribute to the bonding interactions. It implies that the system will become unstable due to lithium reduction and the oxygen atoms adjacent to Ni will be easier to be removed, which is in consistence with our previous conclusion.

The formation of Li/Ni antisites might be in the following way: delithiation leads the concentration of oxygen vacancy

defects to increase, and the high concentration of oxygen vacancy defects makes Ni atoms lose the binding of the O atoms at both ends and diffuse into the Li sites, which finally form the Li/Ni antisites.

4. Conclusions

In this work, we investigated the structural stability of Li_xNiO_2 by using the first-principles approach, with consideration of the effect of oxygen vacancy and the Li–Ni antisite. We determine the ground states of the layered $LiNiO_2$ material corresponding to concentrations of 1/4, 2/5, 3/7, 1/2, 2/3, 3/4, 5/6, and 6/7, respectively, and the calculated voltage curves are in good agreement with the measured voltage curves. The oxygen vacancy formation energy of Li_xNiO_2 is 0.6 eV for an Li concentration of 25%, and it further decreases by 0.2 eV after the oxygen vacancy concentration has reached 3%. The stability of the material will be severely reduced, and the precipitation of oxygen will increase the probability of causing safety accidents. When the oxygen vacancy concentration reaches 12.5%, the formation energy of Li/Ni antisite will become negative, and then the antisite will occur, hindering Li diffusion and leading to a significant decrease of capacity.

Acknowledgements

Project supported by the Science Fund of the Guangdong Major Project of Basic and Applied Basic Research, China (Grant No. 2019B030302011) and the Fund of the Science and Technology Program of Guangzhou, China (Grant No. 202201010090).

References

[1] Dunn B, Kamath H and Tarascon J M 2011 *Science* **334** 928
[2] Goodenough J B 2014 *Energy Environ. Sci.* **7** 14
[3] Seong W M and Manthiram A 2021 *Energy Storage Materials* **34** 250
[4] Mock M, Bianchini M, Fauth F, Albe K and Sicolo S 2021 *J. Mater. Chem. A* **9** 14928
[5] Liu W, Oh P, Liu X, Lee M J, Cho W, Chae S, Kim Y and Cho J 2015 *Angew. Chem. Int. Ed.* **54** 4440
[6] Li J, Downie L E, Ma L, Qiu W and Dahn J R 2015 *J. Electrochem. Soc.* **162** A1401
[7] Bak S M, Hu E, Zhou Y, Yu X, Senanayake S D, Cho S J, Kim K B, Chung K Y, Yang X Q and Nam K W 2014 *ACS Appl. Mater. Interfaces* **6** 22594
[8] Min K, Kim K, Jung C, Seo S W, Song Y Y, Lee H S, Shin J and Cho E 2016 *Journal of Power Sources* **315** 111
[9] Kowalski P M, Bornhake T, Cheong O, Dohrmann N, Koch Liston A L, Potts S K, Shad A, Tesch R and Ting Y Y 2023 *Front. Energy Res.* **10** 1096190
[10] Spotnitz R and Franklin J 2003 *Journal of Power Sources* **113** 81
[11] Bandhauer T M, Garimella S and Fuller T F 2011 *J. Electrochem. Soc.* **158** R1
[12] Wang L, Maxisch T and Ceder G 2007 *Chem. Mater.* **19** 543
[13] Min K, Seo S W, Song Y Y, Lee H S and Cho E 2017 *Phys. Chem. Chem. Phys.* **19** 1762
[14] Kang K, Meng Y S, Bréger J, Grey C P and Ceder G 2006 *Science* **311** 977
[15] Guilmard M 2003 *Journal of Power Sources* **115** 305
[16] Kresse G and Hafner J 1993 *Phys. Rev. B* **47** 558
[17] Kresse G and Hafner J 1994 *Phys. Rev. B* **49** 14251
[18] Kresse G and Furthmüller J 1996 *Computational Materials Science* **6** 15
[19] Kresse G and Furthmüller J 1996 *Phys. Rev. B* **54** 11169
[20] Blöchl P E 1994 *Phys. Rev. B* **50** 17953
[21] Perdew J P, Burke K and Ernzerhof M 1996 *Phys. Rev. Lett.* **77** 3865
[22] Wang L, Maxisch T and Ceder G 2006 *Phys. Rev. B* **73** 195107
[23] Jain A, Hautier G, Moore C J, Ping Ong S, Fischer C C, Mueller T and Persson K A, Ceder G 2011 *Comput. Mater. Sci.* **50** 2295
[24] He C C, Liao J H, Qiu S B, Zhao Y J and Yang X B 2021 *Comput. Mater. Sci.* **193** 110386
[25] Cen Y J, He C C, Qiu S B, Zhao Y J and Yang X B 2022 *Phys. Rev. Mater.* **6** L050801
[26] Stefan Maintz, Volker L. Deringer, Andrei L. Tchougreeff and Richard Dronskowski 2016 *J. Comput. Chem.* **37** 1030
[27] Arroyo y de Dompablo M E, Van der Ven A and Ceder G 2002 *Phys. Rev. B* **66** 064112
[28] Das H, Urban A, Huang W and Ceder G 2017 *Chem. Mater.* **29** 7840
[29] Aydinol M K, Kohan A F, Ceder G, Cho K and Joannopoulos J 1997 *Phys. Rev. B* **56** 1354
[30] Liu L, He C C, Zeng J, Peng Y H, Chen W Y, Zhao Y J and Yang X B 2021 *J. Phys. Chem. C* **125** 7077